2019

# Bipedal Model and Hybrid Zero Dynamics of Human Walking with Foot Slip

Mitja Trkov
*Rowan University*, trkov@rowan.edu

Kuo Chen

Jingang Yi



## Recommended Citation

Trkov, M., Chen, K., & Yi, J. (2019). Bipedal model and hybrid zero dynamics of human walking with foot slip. ASME Journal of Computational and Nonlinear Dynamics. doi: 10.1115/1.4043360

Journal of Computational and Nonlinear Dynamics. Received August 08, 2018;
Accepted manuscript posted April 04, 2019. doi:10.1115/1.4043360


# Bipedal Model and Hybrid Zero Dynamics of Human Walking with Foot Slip

**Mitja Trkov***
Department of Mechanical Engineering
University of Utah
Salt Lake City, UT 84112, USA
Email: m.trkov@utah.edu

**Kuo Chen***
Department of Mechanical
and Aerospace Engineering
Rutgers University
Piscataway, NJ 08854, USA
Email: kc625@rutgers.edu

**Jingang Yi**†
Department of Mechanical
and Aerospace Engineering
Rutgers University
Piscataway, NJ 08854, USA
Email: jgyi@rutgers.edu



*Foot slip is one of the major causes of falls in human locomotion. Analytical bipedal models provide an insight into the complex slip dynamics and reactive control strategies for slip-induced fall prevention. Most of the existing bipedal dynamics models are built on no foot slip assumption and cannot be used directly for such analysis. We relax the no-slip assumption and present a new bipedal model to capture and predict human walking locomotion under slip. We first validate the proposed slip walking dynamic model by tuning and optimizing the model parameters to match the experimental results. The results demonstrate that the model successfully predicts both the human walking and recovery gaits with slip. Then, we extend the hybrid zero dynamics (HZD) model and properties to capture human walking with slip. We present the closed-form of the HZD for human walking and discuss the transition between the non-slip and slip states through slip recovery control design. The analysis and design are illustrated through human walking experiments. The models and analysis can be further used to design and control wearable robotic assistive devices to prevent slip-and-fall.*

## 1 Introduction

Foot slip is one of the major causes for human falls and injuries. Slip-induced falls cause enormous economic and societal costs [1]. The direct costs for non-fatal fall-related injures among US elderly ($\geq$ 65 years) were 19 billion dollars in the year 2000 [1] and increased to over 31 billion in the year 2015 [2]. Among the occupational population in the US, slips, trips and falls represented 27% of all non-fatal occupational injuries in year 2015 [3]. To develop effective fall prevention strategies and technologies, it is critical to understand human locomotion and balance recovery under slip. Modeling of human walking locomotion with slip is an effective approach to assist in the design and control of new wearable assistive devices. Slip-and-fall has been extensively studied in the past two decades, for example, [4, 5] and references therein. Most of these studies focus on human subjects and clinical experiments and a few use human locomotion dynamics to analyze the slipping mechanism. Simulation-based dynamic models are used to study motion stability of slip and fall. In [5], a 7-link, 9-degree-of-freedom (DOF) walking model in the sagittal plane with a 16-element foot model is used to simulate the human reaction control to a novel slip in gait. In [6], a simulation model is optimized with human experiments. Using this model, stability results are obtained and compared with the dynamic balance analyses by a simple invented pendulum model. The 2D musculoskeletal model in the sagittal plane is also discussed in [7] to determine the impact of the reduced required coefficient of friction (RCOF) on gait kinematics. Kinematic and muscle activity-based data-driven analysis (e.g., Lyapunov exponents) are used to capture the walking stability [8].

Robotic bipedal models [9, 10] were recently presented for study of human walking gait [11, 12], for design of prosthetic devices for lower-limbs [11] and control of robotic walkers. In [13], a bipedal model is proposed to study human gaits with fixed ankle joints. Both the single- and double-stance phases are included in the model and a hybrid zero dynamic control is designed to track the human gait profile. Although the kinematic variables such as hip, knee and HAT (head, arms and trunk) joint angles match the human gaits,

*The authors equally contributed to this work.
†Address all correspondence to J. Yi.

the predicted ground reaction forces (GRFs) have large discrepancies with experiments. In [12], only single-stance locomotion is considered in the model without the HAT. The models in [12, 13] use the circular curved foot-floor contact that was developed in [14]. However, all of the abovementioned bipedal models are built on the assumption that the foot-floor contact friction forces are large enough to prevent the foot from slipping and thus, cannot be directly used to study slip-and-fall walking gaits. Bipedal walking is commonly described by a hybrid dynamics framework with continuous dynamics during the single- or double-stance periods with discrete mappings to capture the foot contact impacts. Using the HZD concept [15], a low-dimensional normal human walking model is presented in [13] and a state feedback control is designed to track the gait profile parameterized by the stance phase variable, rather than time [9]. The repetitive human walking gait is captured by the HZD when the gaits follow the desired profiles.

The goal of this study is to develop an analytic bipedal model and extend the HZD approach for human walking with slip. The model extends the bipedal framework in [9, 11, 12] by relaxing the foot no-slip assumption and using the circular rolling feet to capture the foot rolling characteristics. The proposed human walking model is built on a 7-link robotic bipedal dynamics model with actuated ankle joints. The model includes the dynamics of both the single- and double-stance motion. The model explicitly considers the foot slipping displacement and therefore, can predict the human gait under slips. Moreover, we explicitly calculate and present the HZD that consists of dynamics of the gait progression variable and the slipping distance. The inclusion of the latter parameter is new compared to the existing HZD models. The HZD stability conditions and properties are also discussed under a set of slip recovery gaits that are obtained from human subject experiments. This paper extends the previous conference publications [16, 17] by providing additional details in bipedal model derivation, model validation, detailed HZD analyses of slip recovery stability examples and experiments.

The main impact of this work lies in the development of bipedal model and HZD slip analysis that provides an important insight into slip balance recovery analysis. This analytic analysis enables determination of the outcome of the balance recovery and distinguishing between successful vs unsuccessful slip balance recovery, based on a current state/posture and angular momentum of the human model. The slip balance recovery analysis can be used in controller design of wearable robotic assistive devices for slip-and-fall prevention. Information of the required angular momentum for successful slip recovery based on the current states (i.e., joint angles, foot placement, COP, etc.) can be used to determine the required assistive torques provided by the device or re-positioning of the foot placement to prevent falls.

The measurement of slipperiness and the devices to obtain the shoe-floor friction are discussed in [18]. Force plate is the most commonly used device to measure the GRF and used to calculated the foot contact center of pressure (COP). However, force plates cannot be used for monitoring daily activities outside the laboratory. In recent years, wearable insole pressure measurement devices were developed to obtain the GRF (e.g., [19, 20]). In this work, we use an integrated sensor suite inside each shoe to measure the 3D GRF and torques. The details of these sensors are discussed in [21]. Combining with the wearable motion sensors (e.g., [22]), we obtain the limb poses and forces in indoor or outdoor environments.

The results in this paper complement the existing literature on human bipedal models and gait control. The main contributions of this work are threefold. First, this work extends the robotic bipedal models to study human walking under foot slip. The new model not only predicts the human gait with slip, but also helps to understand the motion stability during slip. Second, besides relaxing the assumption of non-slip foot-floor contact, the new model brings innovative features and properties compared with the existing bipedal models. For example, compared with the bipedal models with a point, a flat or multi-contact foot in [9, 23–25], the new model includes an experimentally validated foot-floor contact circular shaped foot. Unlike the bipedal model in [12] that only deals with a single-stance human locomotion, the proposed model includes the human trunk (e.g., 7-link) and also the double-stance phase, which is crucial for slips and fall motion. Compared with the work in [11, 13], the proposed model includes the active ankle joints and also generates the matched GRF with the experiments. Third, we present the new HZD model and its application to human walking under foot slip. The HZD can be used to analytically investigate the slip balance stability and recovery strategies that are otherwise not possible through clinical studies.

The rest of the paper is organized as follows. We first present the bipedal dynamic model for normal walking gait without slip in Section 2. In Section 3, we present the bipedal model for walking with slips. Section 4 presents hybrid zero dynamics for no-slip walking and slip gait. The experiments and results are presented in Section 5. The discussion of the results is presented in Section 6. We conclude the paper and discuss the future work in Section 7.

## 2 Bipedal Walking Model without Slips

### 2.1 System Configuration

Fig. 1(a) illustrates the setup of the coordinates for bipedal modeling of human walking. The human motion is considered only in the sagittal plane. The human body is considered as a seven-link rigid body. The HAT is considered as one link that is connected to the left- and right-thigh. The model has two active hip joints, two active knee joints and two active ankle joints. Similar to those in [12], we use relative angles $q_i$, $i = 2, \ldots, 7$, to define the configuration of the system and the absolute angle $q_1$ denotes the leading stance leg orientation with respect to the vertical position.

We define the joint angle vector $q_a = [q_1 \ \cdots \ q_7]^T$. The foot-floor contact is considered as a circular disk with radius $R$ rolling on the solid ground; see Fig. 1(b). To capture the slip motion of the foot, we denote the position of the rotating center $O_r$ of the foot as $[x_o \ y_o]^T$ and a slipping vector $q_s =$

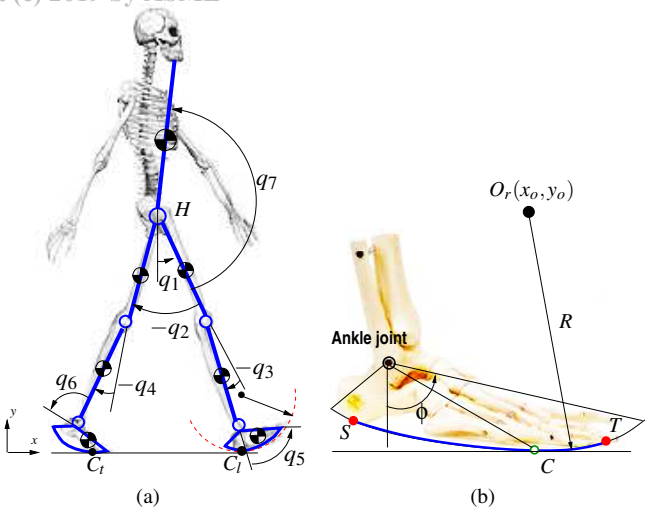


Fig. 1. (a) Schematic of the 7-link human walking model with curved foot contact. (b) Schematic of the foot-contact model.

$[x_s, y_s]^T = [x_o + R(\phi - \phi_0), y_o - R]^T$, where $\phi$ is the absolute rolling angle of the stance foot with respect to the vertical direction and $\phi_0$ is the initial value of $\phi$. $\dot{q}_s = [\dot{x}_o + R\dot{\phi}, \dot{y}_o]^T$ is the slipping velocity. When the stance foot is purely rolling on the ground, $\dot{q}_s = 0$. We use $q_s$ and $q_a$ (i.e., foot rotating angle) to calculate the stance foot-floor contact point $C$. To completely determine the walking gait with slip, we define the generalized coordinate $q_e = [q_a^T \; q_s^T]^T$.

A human walking cycle consists of a series of repeated sequential movements and events [9], namely a single-stance, a double-stance and the foot impact phases. During the single-stance phase, the stance foot rolls on the ground, while the swing foot moves in the air from positions behind to front of the stance foot. Once the swing foot impacts on the ground (i.e., heel-touch), the joint velocity suddenly changes and the joint configuration is relabeled due to the switching role of the stance and swing legs. The double-stance phase refers to the stage when both legs roll on the ground. Finally, the trailing stance foot leaves the ground (i.e., toe-off) and the pose returns to the single-stance phase. Hybrid models shown in Fig. 2 are used to capture the above-mentioned discrete-continuous dynamics.

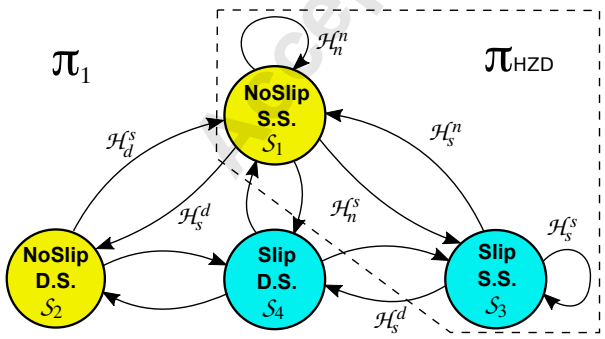


Fig. 2. Finite state diagram of human walking gait with slips.

### 2.2 Single- and Double-Stance Models and Gait Controller

The non-slip single-stance dynamics are described as [9]

$$\Sigma_s: \; D_s(q_a)\ddot{q}_a + C_s(q_a, \dot{q}_a)\dot{q}_a + G_s(q_a) = B_s u, \qquad (1)$$

where $D_s(q_a)$, $C_s(q_a, \dot{q}_a)$, $G_s(q_a)$ and $B_s$ are the inertia, Coriolis, gravity and input mapping matrices, respectively. There are six joint torque inputs $u \in \mathbb{R}^6$ and the system is underactuated since absolute joint angle $q_1$ is not controlled by any joint torque.

Therefore, we have $B_s = [0_{n-1} \; I_{n-1}]^T$, where $0_n = [0 \cdots 0]^T \in \mathbb{R}^n$ is a zero column vector and $I_n$ is an $n$-dimensional identity matrix, where $n$ represents a total number of joint angles ($n = 7$ in this paper). A feedback linearization approach is adopted to control the joint angles $q_a$ to follow a desired trajectory that is specified by a progression variable $\theta = cq_a$, where $c$ is a constant progression vector. During the single-stance phase, $\theta$ monotonically increases and the desired trajectory of actuated joint angles are expressed by $\theta$. The feedback linearization controller enforces the virtual constraint specified by

$$y = h(q_a) = H_0 q_a - h_d(\theta) = 0, \qquad (2)$$

where $H_0$ is a constant matrix and $h_d(\theta)$ is the desired trajectories of actuated joint angles described by the Bézier polynomials [9]. If $u$ is properly chosen by feedback linearization to drive $y = \dot{y} = 0$, only the dynamics of $\theta$ is left as the zero dynamics [9].

To calculate the GRF for single-stance walking, we consider the dynamics of the individual link expressed as a function of joint angles, angular velocities and accelerations. We sum these contributions to compute the instantaneous horizontal and vertical accelerations of the center of mass using forward kinematics. The external forces acting on the center of mass are the ground reaction forces and the gravitational force. Using Newtonian mechanics it is straightforward to obtain the normal $F_n$ and tangential force $F_x$ at foot/ground contact points. This force calculation method is also generalized to the single-stance slip case discussed in Section 3.2.

During the double-stance phase, both the leading and trailing feet are in contact with the ground at contact points $C_l$ and $C_t$, respectively; see Fig. 1(a). We consider a general modeling approach by defining slipping vectors $g_l(q_e) \in \mathbb{R}^2$ and $g_t(q_e) \in \mathbb{R}^2$ of contact points $C_l$ and $C_t$, respectively. Note that both $g_l(q_e)$ and $g_t(q_e)$ are determined as functions of $q_e$. Because of the foot-floor contact constraints, the equations of motion during the double-stance are expressed as

$$\Sigma_d: \; D_e(q_e)\ddot{q}_e + C_e(q_e, \dot{q}_e)\dot{q}_e + G_e(q_e) = B_e u + E_e^T F_e, \quad (3)$$

where $D_e(q_e)$, $C_e(q_e, \dot{q}_e)$, $G_e(q_e)$ and $B_e$ are the inertia, Coriolis, gravity and input mapping matrices, respectively. Matrix $E_e = [\frac{\partial g_t(q_e)}{\partial q_e} \; \frac{\partial g_l(q_e)}{\partial q_e}]^T \in \mathbb{R}^{4\times 9}$ describes the contact constraints and $F_e = [F_{xt} \; F_{nt} \; F_{xl} \; F_{nl}]^T$ is a vector of the collection

of the tangential and normal forces at $C_t$ and $C_l$, respectively. With non-slip conditions at $C_l$ and $C_t$, we have four kinematic constraints $E_e\dot{q}_e = 0$ and the degree of freedom given by (3) is $9-4=5$.

Since there are six active joints and five degrees of freedom, the bipedal system is overactuated. Using a similar derivation as in [13], the constrained dynamics is reformulated as

$$D_{di}\ddot{q}_{di} + C_{di}\dot{q}_{di} + G_{di} = M_{di}u, \tag{4}$$

where subscript "di" denotes double-stance independent variable dynamics and $q_{di} = [q_1\ q_2\ q_3\ q_5\ q_7]^T$ and $M_{di} \in \mathbb{R}^{5\times 6}$ maps the six joint torques into the five dimensional dynamics. To predict double-stance human gaits by (4), a Bézier polynomial is used to parameterize the desired trajectory of $q^d_{di}$ [9]. The control input $u$ is designed such that $\ddot{q}_{di} = D^{-1}_{di}(M_{di}u - C_{di}\dot{q}_{di} - G_{di}) = \ddot{q}^d_{di} - K_p(q_{di} - q^d_{di}) - K_d(\dot{q}_{di} - \dot{q}^d_{di})$, where $K_p$ and $K_d$ are constant gain matrices. To solve $u$ in the above equation, we need an additional constraint because of the overactuation configuration. In our implementation, we assume a simple linear constraint of the joint torques $\rho^T u = 0$, and $\rho \in \mathbb{R}^6$ is determined by the single-stance joint torque profiles. This constraint is based on the underlying physical principle assumption that humans minimize the effort for walking. The linear constraint $\rho^T u = 0$ is equivalent to minimizing the effort $u^T(\rho\rho^T)u$.

To calculate the ground reaction forces $F_e$, we take time derivative of the kinematic constraint $E_e\dot{q}_e = 0$. Stacking with the dynamics in (3), we obtain (argument variables in the coefficient matrices are dropped for clarity)

$$\underbrace{\begin{bmatrix} D_e & -E_e^T \\ E_e & 0 \end{bmatrix}}_{D_{\text{ext}}} \begin{bmatrix} \ddot{q}_e \\ F_e \end{bmatrix} = \begin{bmatrix} B_e \\ 0 \end{bmatrix} u - \begin{bmatrix} C_e \\ \dot{E}_e \end{bmatrix} \dot{q}_e - \begin{bmatrix} G_e \\ 0 \end{bmatrix}. \tag{5}$$

Since matrix $D_{\text{ext}}$ is full rank, both $\ddot{q}_e$ and forces $F_e$ are obtained with the known $u$ from the above controller design.

### 2.3 Impacting Model

The impact dynamics are obtained by integrating the double stance dynamics equation (3) over the instantaneous impact time with certain neglections [9]

$$D_e(q_e^-)\dot{q}_e^+ - D_e(q_e^-)\dot{q}_e^- = E_{el}^T(q_e^-)\delta F_{el} + M,$$

where superscripts "+" and "−" indicate the instants just after and before the impact event, respectively. The impulse due to the impact on the leading foot is $\delta F_{el} = \int_{0^-}^{0^+} F_{el}(t)dt$, where $F_{el}$ contains both the normal and tangential ground reaction forces. The GRF applied on the trailing foot $F_{et}$ is not an impact force. The integration of Coriolis term $C_e$ and the gravitational term $G_e$ are relatively small and therefore neglected. The integration of input torque $M = \int_{0^-}^{0^+} B_e u(t)dt$ is a constant determined from the experimental data. After the impact, the swing leg sticks on the ground and thus,

$$E_{el}\dot{q}_e^+ = 0,$$

where $E_{el}(q_e) = \frac{\partial \dot{g}_l}{\partial \dot{q}_e}(q_e)$ is the Jacobian matrix of impacting foot contact point velocity $\dot{g}_l$ with respect to $\dot{q}_e$.

We clearly express the impact mapping $\mathcal{H}_s^d$ as the pre-impact joint velocity $\dot{q}_e^-$ of the single-stance phase to the post-impact joint velocity $\dot{q}_e^+$ of the double-stance phase as

$$\mathcal{H}_s^d:\ \begin{bmatrix} D_e(q_e^-) & -E_{el}^T \\ E_{el} & 0 \end{bmatrix} \begin{bmatrix} \dot{q}_e^+ \\ \delta F_{el} \end{bmatrix} = \begin{bmatrix} D_e(q_e^-)\dot{q}_e^- \\ 0 \end{bmatrix} + \begin{bmatrix} M \\ 0_2 \end{bmatrix}. \tag{6}$$

For periodic walking gait, $M$ can be neglected due to the insignificant input torque $u$ applied during the impact time. However, for slip recovery process, $M$ cannot be neglected for the intentional effort to keep balance.

The matrix on the left-hand side of (6) is invertible and after considering the relabeling of stance foot, we have

$$\dot{q}_a^+ = \Delta_n(q_e^-)\dot{q}_e^- + b_n, \tag{7}$$

where $\Delta_n$ is the impact mapping calculated from (6) and $b_n$ is a constant vector that is related to $M$. Because the new stance foot sticks to the ground, $\dot{q}_e^+ = [(\dot{q}_a^+)^T\ 0_2]^T$ and if the previous step is also non-slip, $\dot{q}_e^- = [(\dot{q}_a^-)^T\ 0_2]^T$. More detailed discussion can be found in [9, 12].

Same as [9, 13], a relabeling process is applied to the joint angles and their velocities after the impact. For the transition from the double-stance to single-stance phases, the transition is obtained as

$$\mathcal{H}_d^s:\ q_e^+ = q_e^-,\ \dot{q}_e^+ = \dot{q}_e^-. \tag{8}$$

### 2.4 Model Optimization for Human Walking Gait

To apply the bipedal model to human gait, we need to tune the model parameters to fit the human walking data. During the human walking experiments, all joint angles and the GRF information are collected and obtained [21, 22].

For single-stance dynamics (1), we need to identify and match the virtual constraint $h(q_a)$ in (2) from the collected joint angles. We use $H_0 = [0\ I_6]$, to choose the active joints [9]. The desired trajectory $h_d$ is parameterized by the Bézier polynomial. To fit the double-stance model (3), we choose to optimize the Bézier spline parameters $\alpha_d$ such that the desired trajectory $q^d_{di} = q^d_{di}(\alpha_d, t)$ approximates human walking and also avoids unrealistic high joint-angular acceleration. We take the joint angular acceleration into the optimization process because the GRF matching is one of the targets besides the joint angles matched. Therefore, we minimize the following objective function

$$J_d(\alpha_d) = \int_{t_0}^{t_f} \|q^d_{di}(\alpha_d, t) - q^e_{di}\|^2 + \gamma\|\ddot{q}^d_{di}(\alpha_d, t)\|^2 dt, \tag{9}$$

where $\gamma > 0$ is a weighting factor and $[t_0,\ t_f]$ is the time interval and $q^e_{di}$ is the measured joint angle profiles. By the property of the Bézier polynomials, we analytically express both $q^d_{di}$ and $\ddot{q}^d_{di}$ as functions of $\alpha_d$ and therefore, the optimal $\alpha_d$ is obtained using a scaled conjugate gradient method. We will demonstrate the results in Section 5.

While in general it is possible to use arbitrary function to parametrize the joint angle trajectories, we specifically chose to use the Bézier polynomials, due to their wide use in modeling smooth curves that requires only few parameters particularly for biped walking model [9]. We particularly chose fifth-order Bézier polynomials that are determined by six points. Two of these are determined as the starting and end points of the joint angle trajectory that are determined from the experiments. This simplifies the parameter estimation process. The remaining parameters are tuned based on minimizing the objective function $J_d(\alpha_d)$.

## 3 Bipedal Walking Model with Foot-Floor Contact Slip

In this section, we extend the bipedal model in the previous section to consider the foot-floor contact slip. We first present an overview of the extended hybrid model and the detailed dynamics are then discussed.

### 3.1 Hybrid Model for Walking with Slip

Fig. 2 shows the finite state diagram of the hybrid bipedal model for human walking with foot-floor contact slip. For the normal walking gait, the hybrid dynamics contain two states: non-slip single-stance and double-stance phases shown as $\mathcal{S}_1$ and $\mathcal{S}_2$, respectively. The heel-touch and toe-off events trigger the switching between $\mathcal{S}_1$ and $\mathcal{S}_2$ with the impact mappings $\mathcal{H}^d_s$ and $\mathcal{H}^s_d$, respectively.

The foot slip can happen during the single- and double-stance phases. Therefore, two new states are introduced for the gaits with slip: single-stance slip phase $\mathcal{S}_3$ and double-stance slip phase $\mathcal{S}_4$. State $\mathcal{S}_4$ includes the cases when slip happens on the stance leg only, the swing leg only, or both legs simultaneously. The transitions among $\mathcal{S}_1, i = 1,2,3,4$, shown in Fig. 2 represent the human slip recovery strategies. For example, as we will show in the case study in Section 5, one slip recovery strategy can be represented in the sequence of $\mathcal{S}_1 \to \mathcal{S}_4 \to \mathcal{S}_3 \to \mathcal{S}_1$. The details of each transition in the finite state diagram are parts of the required human slip recovery strategies. These slip recovery strategies are out of the scope of this paper and we omit the discussion here.

### 3.2 Single-Stance Slip Model and Gait Controller

Due to foot slip, we use the extended configuration coordinate $q_e = [q_a^T\ q_s^T]^T = [q_a^T\ x_s\ y_s]^T$ to describe the motion. The dynamic model is obtained as

$$\underbrace{\begin{bmatrix} D^{11}_{es} & \vdots & D^{12}_{es} \\ \cdots & \cdots & \cdots \\ D^{21}_{es} & \vdots & D^{22}_{es} \\ \cdots & \cdots & \cdots \\ D^{31}_{es} & \vdots & D^{32}_{es} \end{bmatrix}}_{D_{es}} \begin{bmatrix} \ddot{q}_a \\ \ddot{x}_s \\ \cdots \\ \ddot{y}_s \end{bmatrix} + \underbrace{\begin{bmatrix} C^{11}_{es} & \vdots & C^{12}_{es} \\ \cdots & \cdots & \cdots \\ C^{21}_{es} & \vdots & C^{22}_{es} \\ \cdots & \cdots & \cdots \\ C^{31}_{es} & \vdots & C^{32}_{es} \end{bmatrix}}_{C_{es}} \begin{bmatrix} \dot{q}_a \\ \dot{x}_s \\ \cdots \\ \dot{y}_s \end{bmatrix} + \underbrace{\begin{bmatrix} G^1_{es} \\ G^2_{es} \\ \cdots \\ G^3_{es} \end{bmatrix}}_{G_{es}} = \begin{bmatrix} B_{es}u \\ F_x \\ \cdots \\ F_n \end{bmatrix} = \begin{bmatrix} B_{es}u \\ F_{es} \end{bmatrix}, \tag{10}$$

where $D_{es} \in \mathbb{R}^{9\times 9}$, $C_{es} \in \mathbb{R}^{9\times 9}$, $G_{es} \in \mathbb{R}^9$ and $B_{es} \in \mathbb{R}^{7\times 6}$ are the inertia, Coriolis, gravity and input mapping matrices, respectively. We define matrices $D^{ij}_{es}$, $C^{ij}_{es}$ and $G^{ij}_{es}$, where indexes $i = 1,2,3$ represent respectively the first seven, the eighth and the ninth row and indexes $j = 1,2$ represent respectively the first eighth and the ninth column of the matrices $D_{es}$, $C_{es}$ and $G_{es}$. External force $F_{es} = [F_x\ F_n]^T$ is the frictional (tangential) and normal forces at the stance foot.

The stance foot is always in contact with the ground during slipping (i.e., $y_s = 0$) and therefore, we have constraint $q_s = [x_s\ y_s]^T = [x_s\ 0]^T$. Also, we have $F_x = -\mu F_n$, where $\mu$ is the friction coefficient between the shoe sole and the ground floor. With these constraints, we further simplify (10) by defining new coordinate $q_{es} = [q_a\ x_s]^T \in \mathbb{R}^8$ and eliminating external force $F_n$ and finally obtain

$$\Sigma^s_s:\ D^s_{es}\ddot{q}_{es} + C^s_{es}\dot{q}_{es} + G^s_{es} = B^s_{es}u, \tag{11}$$

where

$$D^s_{es} = \begin{bmatrix} D^{11}_{es} \\ D^{21}_{es} + \mu D^{31}_{es} \end{bmatrix},\ C^s_{es} = \begin{bmatrix} C^{11}_{es} \\ C^{21}_{es} + \mu C^{31}_{es} \end{bmatrix} \in \mathbb{R}^{8\times 8},$$
$$G^s_{es} = \begin{bmatrix} G^1_{es} \\ G^2_{es} + \mu G^3_{es} \end{bmatrix} \in \mathbb{R}^8,\ B^s_{es} = \begin{bmatrix} B_{es} \\ 0 \end{bmatrix} \in \mathbb{R}^{8\times 6}.$$

The system given by (11) has eight state variables and six joint torques as inputs and therefore, it is underactuated. The absolute joint angle $q_1$ and the slipping distance $x_s$ are underactuated variables. To use model (11) for human gait prediction, we adopt a similar controller as for the non-slip case. A six-dimensional holonomic virtual constraint $y = h(q_a) = H_0 q_a - h_d(\theta_s)$ is used to design the control system, where $\theta_s = c_s q_a$ and $c_s$ is chosen to ensure $[H_0^T\ c_s^T]^T$ is full rank. Similar to the non-slip case, letting $\eta = h(q_a)$, the control $u$ is chosen to regulate $\eta = \dot{\eta} = 0$ and the zero dynamics are obtained. Specifically, we define $\xi = \left(D^{11}_{es}\right)_1 \dot{q}_a$, where $\left(D^{11}_{es}\right)_1$ is the first seven elements of the first row of matrix $D^{11}_{es}$ and it corresponds to the unactuated variable $q_1$. The dynamics of $\xi$ and $\dot{x}_s$ are indeed the zero dynamics of the system and will be presented in Section 4. Compared with the non-slip single-stance case, the zero dynamics of the slip walking model contain one additional variable $\dot{x}_s$.

### 3.3 Double-Stance Slip Model and Gait Controller

During the double-stance slip gait, either (i) only one of two feet slips while the other foot purely rolls on the ground, or (ii) both feet slide on the ground. These two situations share the same equations of motion given by (3) but with different governing constraints. For the first case, we always define the non-slipping leg as the stance leg and from the stance leg, we define the absolute joint angle $q_1$; see Fig. 1(a). For the second case, we take either leg as the stance leg.

By such arrangements, for case (i), without loss of generality, we assume that the trailing leg is non-slip and also the stance leg. Therefore, we have kinematic constraints $g_t(q_e) = 0$ and $(g_l(q_e))_y = 0$, where $(g_i(q_e))_j$, $i = l,t$, $j = x,y$, represents the $j$th coordinate of slipping vector $g_i(q_e)$. Moreover, we have the kinetic constraints $F_{xl} = -\mu F_{nl}$ for slipping foot. Similarly, for case (ii), we have the kinematic constraints $(g_t(q_e))_y = (g_l(q_e))_y = 0$ and kinetic constraints $F_{xt} = -\mu F_{nt}$ and $F_{xl} = -\mu F_{nl}$. In the following, we only present the dynamics for case (i) and similar results can be obtained for case (ii).

Because of constraints $g_t(q_e) = 0$ and $(g_l(q_e))_y = 0$, we obtain $\frac{\partial g_t}{\partial q_e}\dot{q}_e = 0$ and $\frac{\partial (g_l(q_e))_y}{\partial q_e}\dot{q}_e = 0$. Using the definition of $E_e$ in (3), these kinematic constraints are written into compact form $E_{es}\dot{q}_e = 0$, where $E_{es} := (E_e)_{[1,2,4]} \in \mathbb{R}^{3\times 9}$ is a matrix formed by taking rows $1,2$ and $4$ of $E_e$. Similarly, the kinetic constraint $F_{xl} = -\mu F_{nl}$ is used to re-write the external force vector in (3) as

$$F_e = \underbrace{\begin{bmatrix} 1 & 0 & 0 \\ 0 & 1 & 0 \\ 0 & 0 & -\mu \\ 0 & 0 & 1 \end{bmatrix}}_{C_f} \underbrace{\begin{bmatrix} F_{xt} \\ F_{nt} \\ F_{nl} \end{bmatrix}}_{F_{e3}} = C_f F_{e3}. \tag{12}$$

Similar to the treatment to obtain (5), by taking derivative of velocity constraint $E_{es}\dot{q}_e = 0$ and stacking with the simplified (3) and (12), we obtain

$$\underbrace{\begin{bmatrix} D_e & -E_e^T C_f \\ E_{es} & 0 \end{bmatrix}}_{D^s_{\text{ext}}} \begin{bmatrix} \ddot{q}_e \\ F_{e3} \end{bmatrix} = \underbrace{\begin{bmatrix} B_e \\ 0 \end{bmatrix}}_{B^s_{\text{ext}}} u - \underbrace{\begin{bmatrix} C_e \\ \dot{E}_{es} \end{bmatrix} \dot{q}_e - \begin{bmatrix} G_e \\ 0 \end{bmatrix}}_{C^s_{\text{ext}}}.$$

Matrix $D^s_{\text{ext}}$ is full rank and therefore $\ddot{q}_e$ and $F_{e3}$ are uniquely determined once the current state variables and joint torques $u$ are given. Since the three dimensional constraints $E_{es}\dot{q}_e = 0$ are enforced, the degrees of freedom of the system are $9-3=6$. Therefore, the system is fully actuated.

Letting $q_i = [q_1\, q_2\, q_3\, q_4\, q_5\, q_7]^T = Sq_e$ be the independent variables, where $S \in \mathbb{R}^{6\times 9}$ is a constant transformation matrix from $q_e$ to $q_i$, we express $\ddot{q}_i = S(D^s_{\text{ext}}{}^{-1} B^s_{\text{ext}} u + D^s_{\text{ext}}{}^{-1} C^s_{\text{ext}})$, where $SD^s_{\text{ext}}{}^{-1} B^s_{\text{ext}} \in \mathbb{R}^{6\times 6}$ is a full rank matrix. To track a given trajectory $q_i^d$, the controlled joint torque is designed as $u = (SD^s_{\text{ext}}{}^{-1} B^s_{\text{ext}})^{-1}(\ddot{q}_i^d - K_p(q_i - q_i^d) - K_d(\dot{q}_i - \dot{q}_i^d) - SD^s_{\text{ext}}{}^{-1} C^s_{\text{ext}})$, where $K_p$ and $K_d$ are constant gain matrices.

### 3.4 Impact Model for Walking Gait with Slip

The impact model under slip is obtained from the extension of the non-slip case in Section 2.3. The main difference is that the slip can happen right after the impact and therefore, the velocity of heel-touch contact point $C_l$ is possibly nonzero, unlike zero in non-slip case. From the discussion in the previous sections, we have the velocity constraint $E_e\dot{q}_e = v_{\text{slip}} = [0\ 0\ v_{\text{slip}}\ 0]^T$, where $v_{\text{slip}}$ is the slipping velocity of point $C_l$ (along the $x$-axis direction) after the heel-touch impact. Therefore, we obtain

$$\mathcal{H}^s_n : \begin{bmatrix} D_e(q_e^-) & -E_e^T \\ E_e & 0 \end{bmatrix} \begin{bmatrix} \dot{q}_e^+ \\ \delta F_e \end{bmatrix} = \begin{bmatrix} D_e(q_e^-)\dot{q}_e^- \\ v_{\text{slip}} \end{bmatrix}. \tag{13}$$

Compared with (6), one more unknown $\dot{x}_s^+$ is introduced. We here use the friction coefficient to relate impulses $F_{2x} = -\mu F_{2y}$ because of the friction model and the integration over instantaneous impact time. Considering relabeling, we have

$$\dot{q}_e^+ = \begin{bmatrix} \dot{q}_a^+ \\ \dot{x}_s^+ \\ 0 \end{bmatrix} = \Delta_s(q_e^-)\dot{q}_e^-, \tag{14}$$

where $\Delta_s$ denotes the foot-slip impact mapping matrix.

## 4 Hybrid Zero Dynamics of Slip Recovery

In this section, we first present the HZD for bipedal walking with foot slip. Then, we discuss a set of slip recovery phases that are observed in the experiments. Finally, we introduce the stability of slip recovery sequence. Since single-stance phase takes main stance gait duration and due to the complexity of the double-stance dynamics, only single-stance dynamics are considered in the HZD analysis. This simplification helps highlight the HZD of slip recovery process in later discussion, and also allows us to consider only the continuous non-slip and slip dynamics, $\mathcal{S}_1$ and $\mathcal{S}_3$, and their respective impact mapping transitions. For completeness, two additional return impact mappings are required: $\mathcal{H}^n_l$ and $\mathcal{H}^s_s$ transitions back to the non-slip single-stance phase ($\mathcal{S}_1$) and the slip single-stance ($\mathcal{S}_3$), respectively. These are all defined in domain $\pi_{HZD}$ as shown in Fig. 2.

### 4.1 Zero Dynamics of Non-Slip Single-Stance Phase

The non-slip single-stance zero dynamics is obtained by enforcing the states of (1) onto the virtual constraint (2). Following a similar treatment in [12], we define $x_a = [q_a^T\ \dot{q}_a^T]^T$ and re-write (1) into a first-order form

$$\dot{x}_a = f(x_a) + g(x_a)u, \tag{15}$$

where $f(x_a) = \begin{bmatrix} \dot{q}_a \\ -D_s^{-1}(C_s\dot{q}_a + G_s) \end{bmatrix}$, $g(x_a) = \begin{bmatrix} 0_{7\times 6} \\ D_s^{-1}B_s \end{bmatrix}$. We consider a coordinate transformation

$$\eta_1 = h(q_a), \eta_2 = L_f h(q_a), \xi_1 = \theta(q_a), \xi_2 = D_a(q_a)\dot{q}_a, \tag{16}$$

where $L_f h(q_a)$ is the Lie derivative of $h(q_a)$ along $f$, and $D_a(q)$ is formed by the row of $D_s(q)$ that corresponds to the unactuated joint angle $q_1$. Choosing $u = (L_g L_f h)^{-1}(-L_f^2 h + v)$ and $v$ to regulate $\eta_1 = \eta_2 = 0$ exponentially, the output dynamics become $\dot{\eta}_1 = \eta_2$, $\dot{\eta}_2 = v$. The zero dynamics is given as

$$\Sigma_{ZD}^n : \begin{cases} \dot{\xi}_1 = \frac{\partial \theta}{\partial q_a}\dot{q}_a =: k_1(\xi_1)\xi_2, \\ \dot{\xi}_2 = \dot{q}_a^T \frac{\partial D_a^T}{\partial q_a}\dot{q}_a - C_a\dot{q}_a - G_a =: k_2(\xi_1, \xi_2). \end{cases} \tag{17}$$

The transformation of output $\eta := [\eta_1^T \ \eta_2^T]^T$ and internal states $\xi := [\xi_1 \ \xi_2]^T$ to $x_a$ is obtained as

$$\begin{bmatrix} \eta_1 \\ \xi_1 \end{bmatrix} = \begin{bmatrix} h(q_a) \\ \theta(q_a) \end{bmatrix} =: \Phi(q_a), \begin{bmatrix} \eta_2 \\ \xi_2 \end{bmatrix} = \begin{bmatrix} \frac{\partial h(q_a)}{\partial q_a} \\ D_a(q_a) \end{bmatrix} \dot{q}_a, \tag{18}$$

and the inverse transformation is

$$q_a = \Phi^{-1}\left(\begin{bmatrix} \eta_1 \\ \xi_1 \end{bmatrix}\right), \dot{q}_a = \begin{bmatrix} \frac{\partial h(q_a)}{\partial q_a} \\ D_a(q_a) \end{bmatrix}^{-1} \begin{bmatrix} \eta_2 \\ \xi_2 \end{bmatrix}. \tag{19}$$

When $\eta = 0$, $x_a$ is a function of only $\xi$ and the right-hand side of (17) can be written as function of $\xi$.

To maintain stable gaits, the pre-impact states should be mapped to zero dynamics space under the impact mapping (7) [9], that is,

$$\Delta_n(S \cap Z_{\alpha_n}) \subset Z_{\alpha_n}, \tag{20}$$

where $S$ is the double-stance configuration space and $Z_{\alpha_n}$ is the single-stance zero dynamics space under normal walking gait profile $\alpha_n$. Assuming the pre-impact zero dynamics state is $\xi^-$, the pre-impact full state is $x_a^-$ by applying (19) with $\eta = 0$. The post-impact state is obtained $x_a^+$ by (7). The hybrid invariant set requires that the after-impact state is still on the zero dynamic space, namely,

$$\eta_1 = h(q_a^+) = 0, \eta_2 = \frac{\partial h}{\partial q_a}(q_a^+)\dot{q}_a^+ = 0.$$

### 4.2 Zero Dynamics of Single-Stance Phase with Slip

The slip single-stance phase dynamics (11) has two degrees of underactuation, i.e., the absolute joint angle $q_1$ and the slip distance $x_s$. The 6-dimension virtual constraint for slip single-stance phase is

$$y = h_s(q_a) = 0. \tag{21}$$

Similar to the non-slip case, defining $x_{es} = [q_{es}^T \ \dot{q}_{es}^T]^T$, (11) is written as

$$\dot{x}_{es} = f_s(x_{es}) + g_s(x_{es})u, \tag{22}$$

where $f_s$ and $g_s$ are similar to those in (15) with corresponding coefficient matrices from $\Sigma_s$ in (11). Defining the state transformation $\eta_s = [\eta_{1s}^T \ \eta_{2s}^T]^T = [h_s(q_a) \ L_{f_s}h_s]^T$, we use the feedback linearization to obtain the output dynamics $\dot{\eta}_{1s} = \eta_{2s}$, $\dot{\eta}_{2s} = w$, where $w$ is the new control input to drive $\eta_s$ to zero exponentially. The zero dynamics states are defined as

$$\xi_{1s} = \theta_s(q_a), \xi_{2s} = D_{esq}^s\dot{q}_{es}, x_{1s} = x_s, x_{2s} = D_{esx}^s\dot{q}_{es}, \tag{23}$$

where $D_{esq}^s$ and $D_{esx}^s$ are the rows in $D_{es}^s$ that correspond to the unactuated angle $q_1$ and slip distance $x_s$, respectively. Note that $D_{es}^s$ does not depend on $x_s$.

Similar to (18), we obtain the transformation between the new coordinates $\eta_s$, $\xi_s$, and $x_s = [x_{1s} x_{2s}]^T$ with the original states $x_{es}$ as

$$\begin{bmatrix} \eta_{1s} \\ \xi_{1s} \\ x_{1s} \end{bmatrix} = \begin{bmatrix} \Phi_s(q_a) \\ x_s \end{bmatrix}, \begin{bmatrix} \eta_{2s} \\ \xi_{2s} \\ x_{2s} \end{bmatrix} = \underbrace{\begin{bmatrix} \frac{\partial h_s}{\partial q_a} & 0 \\ D_{esq}^s(q_a) & \\ D_{esx}^s(q_a) & \end{bmatrix}}_{\lambda(q_a)} \dot{q}_{es} = \lambda(q_a)\dot{q}_{es},$$

where $\Phi_s(q_a) = [h_s \ \theta_s]^T = [\eta_{1s}^T \ \xi_{1s}]^T$ and the inverse transformation is

$$q_{es} = \begin{bmatrix} q_a \\ x_s \end{bmatrix} = \begin{bmatrix} \Phi_s^{-1} \\ x_{1s} \end{bmatrix}, \dot{q}_{es} = \lambda^{-1}(q_a) \begin{bmatrix} \eta_{2s} \\ \xi_{2s} \\ x_{2s} \end{bmatrix}. \tag{24}$$

The zero dynamics is given as

$$\begin{aligned} \dot{\xi}_{1s} &= \frac{\partial \theta_s}{\partial q_a}\dot{q}_a, \dot{x}_{1s} = \dot{x}_s, \\ \dot{\xi}_{2s} &= \dot{q}_{es}^T \frac{\partial (D_{esq}^s)^T}{\partial q_{es}}\dot{q}_{es} - C_{esq}^s\dot{q}_s - G_{esq}^s =: k_{2s}(\xi_{1s}, \xi_{2s}, x_{2s}), \\ \dot{x}_{2s} &= \dot{q}_{es}^T \frac{\partial (D_{esx}^s)^T}{\partial q_s}\dot{q}_s - C_{esx}^s\dot{q}_s - G_{esx}^s. \end{aligned} \tag{25}$$

From the property of robot motion (10) [26], we obtain

$$C_{esx}^s = \dot{q}_s^T \frac{\partial (D_{esx}^s)^T}{\partial q_s}. \tag{26}$$

We simplify the zero dynamics by substituting (26) into (25) with (24) and $\eta_s = 0$, and obtain

$$\begin{bmatrix}\dot{\xi}_{1s}\\ \dot{x}_{1s}\end{bmatrix} = \begin{bmatrix}\frac{\partial\theta_s}{\partial q_a} & 0\\ 0_N^T & 1\end{bmatrix}\lambda^{-1}(q_a)\begin{bmatrix}0_{N-1}\\ \xi_{2s}\\ x_{2s}\end{bmatrix} =: k_{1s}(\xi_{1s})\begin{bmatrix}\xi_{2s}\\ x_{2s}\end{bmatrix},$$
$$\dot{\xi}_{2s} = k_{2s}(\xi_{1s},\xi_{2s},x_{2s}),\ \dot{x}_{2s} = -G^s_{esx} =: k_{3s}(\xi_{1s}), \qquad (27)$$

where $k_{1s}(\xi_{1s})$ and $k_{3s}(\xi_{1s})$ are defined as the coefficients in the above equations.

### 4.3 Multi-Step Slip Recovery Process and Stability

A slip recovery process can be considered a series of walking gaits. We here use a recovery gait sequence as an example to illustrate the principles and stability of the recovery process and the results can be extended to other gait sequences.

As shown in Fig. 2, considering $\pi_{HZD}$, the normal walking dynamics are described by non-slip continuous dynamics $\mathcal{S}_1$ and transition through non-slip foot impact $\mathcal{H}^n_n$. The normal gait profile (virtual constraints) is denoted by $\alpha_n$. When slip happens, phase $\mathcal{S}_1$ with gait $\alpha_n$ transits through the slip impact $\mathcal{H}^s_n$ to slip single-stance phase $\mathcal{S}_3$. In $\mathcal{S}_3$, human tries to touch down the swing foot as soon as possible to find the new support and the gait is described as $\alpha_s$. Once the swing foot touches down, phase $\mathcal{S}_3$ transits back to phase $\mathcal{S}_1$ through impact $\mathcal{H}^n_s$. A recovery gait profile $\alpha_r$ is adopted during this phase. Finally, the gait is successfully recovered back to $\mathcal{S}_1$ with gait profile $\alpha_n$. From the above description, the slip recovery process is summarized as

$$\mathcal{S}_1(\alpha_n) \xrightarrow{\mathcal{H}^s_n} \mathcal{S}_3(\alpha_s) \xrightarrow{\mathcal{H}^n_s} \mathcal{S}_1(\alpha_r) \xrightarrow{\mathcal{H}^n_n} \mathcal{S}_1(\alpha_n). \qquad (28)$$

Note from Fig. 2 that a stable cyclic gait exists for single-stance slip phase $\mathcal{S}_3$ with gait profile $\alpha_s$ and impact $\mathcal{H}^s_s$. This gait does not happen usually in human walking locomotion because it requires skills to regulate highly dynamic motion under foot slip. One example for such gaits is used in figure skating skills in which both stepping and foot slipping co-exist for stable gaits. To demonstrate the capabilities of the extended HZD, we present the results of skating motion later in Section 5.

The non-slip or slip single-stance zero dynamics controllers only drive the system states onto the zero dynamics space of certain phase. To build a zero dynamics space covering the entire slip recovery process, it is necessary to guarantee that the zero dynamics space is invariant under slip ($\mathcal{H}^s_n$) and recovery impacts ($\mathcal{H}^n_s$). Similar to (20), the following conditions should be satisfied for the recovery sequence in (28)

$$\Delta_s(S\cap Z_{\alpha_n}) \subset Z_{\alpha_s}, \Delta_n(S\cap Z_{\alpha_s}) \subset Z_{\alpha_r}, \Delta_n(S\cap Z_{\alpha_r}) \subset Z_{\alpha_n}, \qquad (29)$$

where $Z_{\alpha_s}$ and $Z_{\alpha_r}$ are the slipping and recover step zero dynamics spaces, respectively.

Assuming pre-impact zero dynamics state under a normal walking gait $\alpha_n$ is given as $\xi^- \in S\cap Z_{\alpha_n}$, the pre-impact full state is then $x_a(\xi^-)$ by applying (19) with $\eta = 0$. After the slip impact (14), the initial full state of slip swing phase is ${x_{es}}^+(\xi^-)$. Condition (29) requires that $\eta_{1s}({x_{es}}^+) = h_{\alpha_s}(q^+_{es}) = 0$ and $\eta_{2s}({x_{es}}^+) = \frac{\partial h_{\alpha_s}}{\partial q_a}(q^+_{es})\dot{q}^+_{es} = 0$. Meanwhile, in the HZD space, after the impact, $[\xi^+_s\ x^+_s]^T \in Z_{\alpha_s}$ is related to the pre-impact state $\xi^- \in S\cap Z_{\alpha_n}$ as

$$\begin{bmatrix}\xi^+_s\\ x^+_s\end{bmatrix} = \begin{bmatrix}\theta_s(q^+_a)\\ D^s_{esq}(q^+_a)\dot{q}^+_{es}\\ x^+_s\\ D^s_{esx}(q^+_a)\dot{q}^+_{es}\end{bmatrix} = \begin{bmatrix}\theta_s(Tq_a(\xi^-_1))\\ D^s_{esq}(Tq_a(\xi^-_1))\Delta_s\dot{q}_a(\xi^-_2)\\ 0\\ D^s_{esx}(Tq_a(\xi^-_1))\Delta_s\dot{q}_a(\xi^-_2)\end{bmatrix}$$
$$=: \delta^s_n(\xi^-), \qquad (30)$$

where $T$ is the relabel matrix and the above equation is obtained by applying (23), (14), and (19).

To compute the ending state in the slip single-stance phase, we integrate (27) with respect to time, until either $\xi_{1s} = \xi^+_{1s}$ (start of the step) or $\xi_{1s} = \xi^-_{1s}$ (ending of the step), which implies respectively either not being able to complete this step and return to the initial configuration of this phase, or a complete step is achieved. We denote the ending state as

$$\begin{bmatrix}\xi^-_{2s}\\ x^-_s\end{bmatrix} = \Psi_s(\xi^+, x^+_s; t_s), \qquad (31)$$

where $\Psi_s(\xi_0, x_0; t)$ represents the solution (flow) of the zero dynamics (27) from initial condition $(\xi_0, x_0)$ at $t = 0$ to $(\xi^-_s, x^-_s)$ at $t = t_s$. At the end of slip single-stance phase, the swing foot impacts on the ground and the slipping foot lifts immediately. The pre-impact zero dynamic state is $[\xi^-_s, x^-_s]^T \in S\cap Z_{\alpha_s}$. The full state is $x_{es}(\xi^-_s, x^-_s)$ according to (24) under condition $\eta_s = 0$. After the stick impact, the initial state of recovery step is $x^+_a$ from (7). Condition (29) requires that $\eta_1 = h_{\alpha_r}(q^+_a) = 0$ and $\eta_2 = \frac{\partial h_{\alpha_r}}{\partial q_a}(q^+_a)\dot{q}^+_a = 0$ [1].

The initial HZD state of the recovery step swing phase $\xi^+ \in Z_{\alpha_r}$ is related to the pre-impact state $[\xi^-_s, x^-_s]^T \in S\cap Z_{\alpha_s}$ as

$$\xi^+ = \begin{bmatrix}\theta(Tq_a(\xi^-_{1s}))\\ D_a(Tq_a(\xi^-_{1s}))(\Delta_n\dot{q}_a(\xi^-_s, x^-_s) + b_n)\end{bmatrix} =: \delta^n_s(\xi^-_s, x^-_s), \qquad (32)$$

where (16), (7) and (24) are used to obtain the above equation. The continuous recovery zero dynamics is described by (17). We solve (17) with respect to time until either $\xi_1 = \xi^+_1$ or $\xi_1 = \xi^-_1$, which indicates either not being able to complete this recovery step and returning to the initial configuration of this phase, or a complete recovery step is achieved respectively. We denote the ending state as $\xi^-_2 = \Phi_{\alpha_r}(\xi^+)$.

[1] We here use the subscript to virtual constraint $h$ to indicate the gait profile $\alpha_r$.

At the end of recovery step, the HZD state is $\xi^- \in S \cap Z_{\alpha_r}$ and the full state is $x_a(\xi^-)$. After the impact, the initial state is $x_a^+$ from (7). Condition (29) requires that $\eta_1 = h_{\alpha_n}(q_a^+) = 0$ and $\eta_2 = \frac{\partial h_{\alpha_n}}{\partial q_a}(q_a^+)\dot{q}_a^+ = 0$. Meanwhile, state $\xi^+ \in Z_{\alpha_n}$ is related to pre-impact state $\xi^- \in S \cap Z_{\alpha_r}$ as

$$\xi^+ = \begin{bmatrix} \theta(Tq_a(\xi_1^-)) \\ D_a(Tq_a(\xi_1^-))(\Delta_n \dot{q}_a(\xi^-) + b_n) \end{bmatrix} =: \delta_n^n(\xi^-), \qquad (33)$$

where (16), (7) and (24) are used to obtain the above equation. Finally, we integrate (17) respectively until either $\xi_1 = \xi_1^+$ to $\xi_1 = \xi_1^-$, which implies either not being able to complete a step and returning to the initial configuration of this step, or a complete step is achieved. We denote the final state as $\xi_2^- = \Phi_{\alpha_n}(\xi^+)$.

The entire slip recovery process is therefore represented by state transiting in the HZD space. Starting from the moment right before the slip impact, the initial zero dynamics state $\xi^- \in S \cap Z_{\alpha_n}$ is mapped by $\delta_n^s$, $\Psi_s$, $\delta_s^n$, $\Phi_{\alpha_r}$, $\delta_n^n$ and $\Phi_{\alpha_n}$ successively. The returned value of $\xi_2$ after the slip recovery process is expressed as the composition of these mappings, namely,

$$\xi_2 = \Phi_{\alpha_n} \circ \delta_n^n \circ \Phi_{\alpha_r} \circ \delta_s^n \circ \Psi_s \circ \delta_n^s(\xi_2^-) =: \rho_s(\xi_2^-). \qquad (34)$$

For stable periodic normal walking gait, choosing Poincaré section as $\xi^- \in S \cap Z_{\alpha_n}$, from [9], the Poincaré first return map has a stable fixed point $\xi_2^-$, namely,

$$\xi_2^- = \Phi_{\alpha_n} \circ \delta_n^n(\xi_2^-) = \rho(\xi_2^-) \qquad (35)$$

and

$$\frac{\partial \rho}{\partial \xi_2}(\xi_2^-) < 1. \qquad (36)$$

These properties guarantee the existence of an invariant region $R \subset S \cap Z_{\alpha_n}$ such that for a given $\xi_2^- \in R$, any $\xi_2 \in R$ satisfies

$$|\rho(\xi_2) - \xi_2^-| \leq |\xi_2 - \xi_2^-|. \qquad (37)$$

In the HZD space, the successful slip recovery to the normal gait is equivalent to $\xi_2 = \rho_s(\xi_2^-) \in R$.

## 5 Experiments and Results

We conducted the indoor walking experiments on a wooden platform. Fig. 3 shows the experimental setup of this study. The human subjects walked on the wooden platform in the laboratory. The human subject was first asked to walk on the platform to become familiar with the testing environment before the slip trial. A portion of the platform was painted with a soap film to create slip and recovery gaits when the subject stepped on the slippery surface. The segment with the reduced coefficient of friction was not noticeable to the subject such that the subject kept the normal gait before slip started.

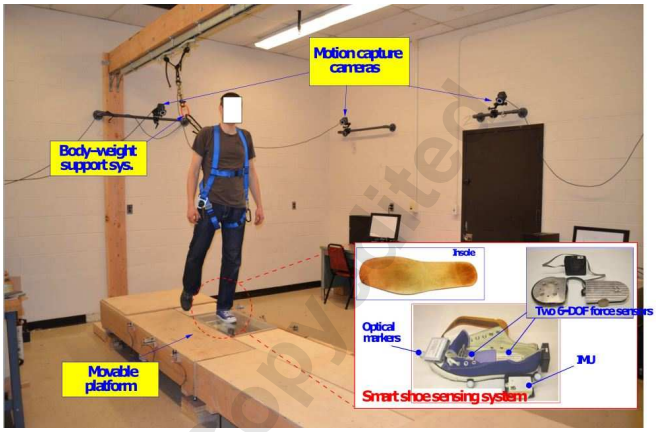


Fig. 3. The slip and fall experimental setup with various sensor suites.

The human walking gait was captured by the optical motion tracking system (8 Bonita cameras from Vicon Inc.) A small wireless inertial measurement unit (from Motion Sense Inc.) was also attached to each shoe to obtain the kinematic information of the foot and potentially for slip detection. Two six degree-of-freedom (6-DOF) force/torque sensors (model SS-1 from INSENCO Co., Ltd) were located inside the shoe to measure the 3D GRF and torques of the foot-floor contact; see Fig. 3. These 6-DOF force sensors are thin (around 12-17 mm in thickness) and the human kept normal walking gait when wearing the shoes with embedded force sensors. The force and torque measurements were transmitted through wireless network to the host computer. The GRF sensors and the motion capture system were synchronized for data collection. The details of discussion about the experimental setup are reported in [21].

We first test and validate the foot rolling geometry using the normal walking motion data. Fig. 4(a) shows the foot center of pressure (COP) trajectory in the ankle frame. The data confirm the circular shape of the rolling model with radius $R = 0.22$ m with its center located at $(0.015, 0.096)$ m in the ankle frame. We use these estimated values in the bipedal model. Fig. 4 shows the comparison results of the seven joint angles by the model prediction and the experiments of normal walking gait. We present these results over a normalized stance $S$ due to the symmetry between the left and right legs. The stance is defined as the time duration from stance foot heel-touch to toe-off. The human subject walks at a speed of around 1.2 m/s and the double-stance consists of around 28% of the entire gait cycle. As shown in Fig. 4, the model predictions (blue solid lines) match the experiments (red dash lines) closely for both the single-stance and double-stance phases. Fig. 5 further shows the comparison results of the GRF (i.e., $F_n$ and $F_x$) of the stance leg. Unlike the diverge

Journal of Computational and Nonlinear Dynamics. Received August 08, 2018;
Accepted manuscript posted April 04, 2019. doi:10.1115/1.4043360


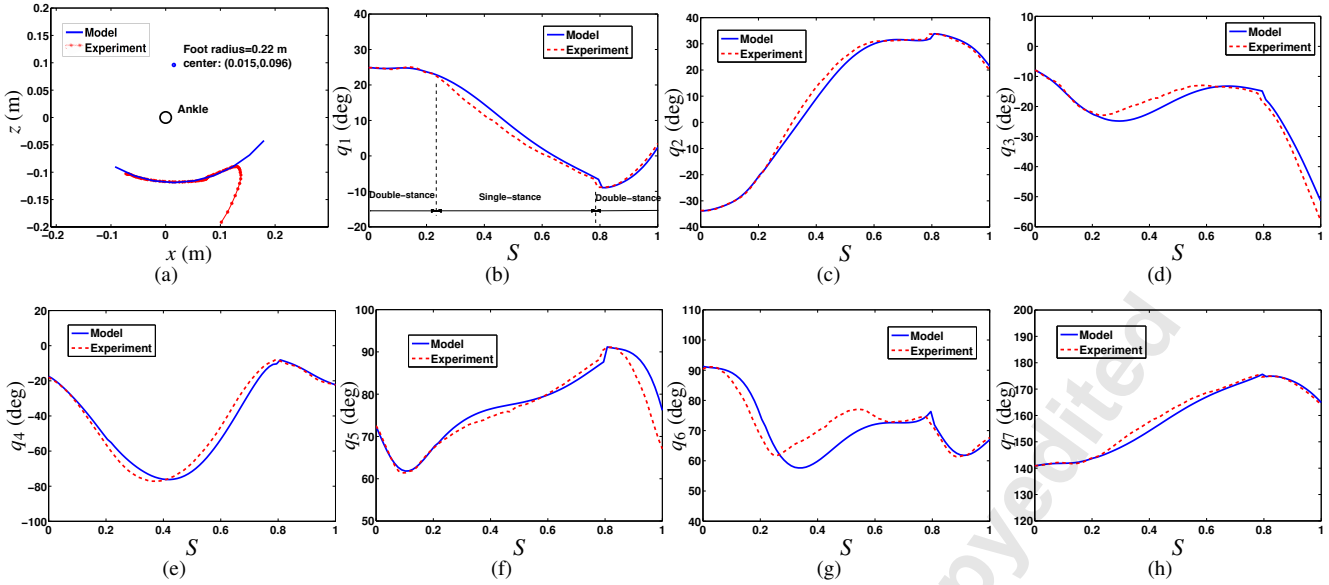


Fig. 4. (a) Experimental data to calculate the foot-floor contact rolling geometry. The red stars indicate the center of pressure (COP) trajectory in the ankle frame and the blue curve is the fitting circular rolling shape. (b)-(h): Joint angle ($q_1$ to $q_7$) comparison between the model prediction and the experiments during normal gait over one stance. The solid lines represent the model predictions and the dash lines show the experimental data.

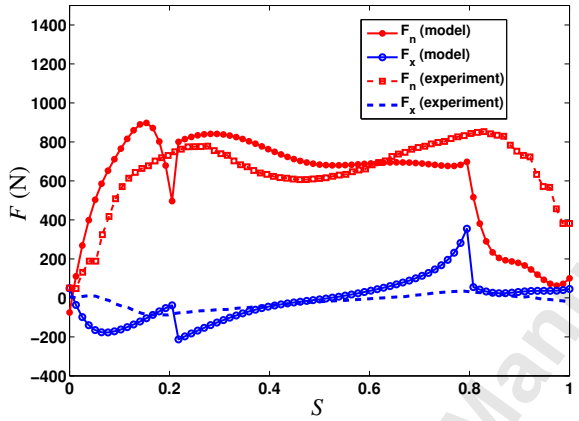


Fig. 5. The GRF ($F_n$ and $F_x$) of the stance leg during the walking gait without slips.

results in literature (e.g., [13]), the model prediction results follow the trend of the measurements from the force sensors. The discontinuity of the predicted GRF takes place at the phase switching moments due to the calculation errors of the joint angle accelerations from the single-stance and the double-stance models.

We next demonstrate the model prediction results for slip recovery gait experiment. Fig. 6(a) shows a video snapshot of the slip recovery gait. The human subject starts the normal gait with a single-stance phase (i.e., $\mathcal{S}_1$ in Fig. 2) at $t = 0$ s. At $t = 0.32$ s, the (left) swing leg touches down on the slippery floor and then starts slipping. At this moment, the (right) foot is still in touch with the floor without slip and the human gait lies in double-stance slip phase ($\mathcal{S}_4$). Then at $t = 0.61$ s, the (right) swing foot leaves the ground (toe-off) and the (left) stance foot still slips. Therefore, the gait enters the single-stance slip phase ($\mathcal{S}_3$). The subject quickly notices and reacts to the slip occurrence. At $t = 0.96$, s the (right) swing foot touches down, the (left) stance foot leaves the ground and the gait becomes a recovered single-stance phase without slipping ($\mathcal{S}_1$). Figs. 6(b) and 6(c) show the human skeleton poses measured by the motion capture system and constructed by the model predicted joint angles, respectively.

Fig. 7 shows the seven joint-angle comparison results of the measurements by the motion capture system and the model predictions considering double-support stance phase. The results clearly confirm that the model prediction follows the experiments closely during the entire gait recovery process. Fig. 7(h) shows the slipping distance results and the model prediction follows the profiles from the experiments. Figs. 8(a) and 8(b) show the normal and tangential GRF for both feet. The GRF comparison shows that except for the double-stance slip phase during $t = 0.32$ s to 0.61 s, the normal and tangential GRF predictions match the measurements. During the double-stance slip period, the force prediction are however not accurate. Possible improvement of these double-stance force calculations could be achieved by increasing the order of the Bézier polynomials, adding additional term in the objective function (9) to follow the COM acceleration with respect to the gait $\alpha_d$ ($\ddot{COM}(\alpha_d)$), or enhancing the GRF distribution between the legs by imposing additional force constraints. Fig. 8(c) shows the required coefficient of friction (RCOF), computed as $RCOF = F_t/F_n$, of the stance-foot contact during the slip recovery process. Before slip starts (at around 0.32 s), the values of RCOF lie in a range of $|RCOF| < 0.2$, which is far less than the available foot-floor friction coefficient (measured close to 1 of the dry rubber-wood contact [21]). At $t = 0.32$ s, the available COF is less than 0.05 due to the soap film on the surface. As shown in Fig. 8(c), the RCOF is nearly constant at around 0.05, which is lower than the available COF. Therefore, slip

Journal of Computational and Nonlinear Dynamics. Received August 08, 2018;
Accepted manuscript posted April 04, 2019. doi:10.1115/1.4043360


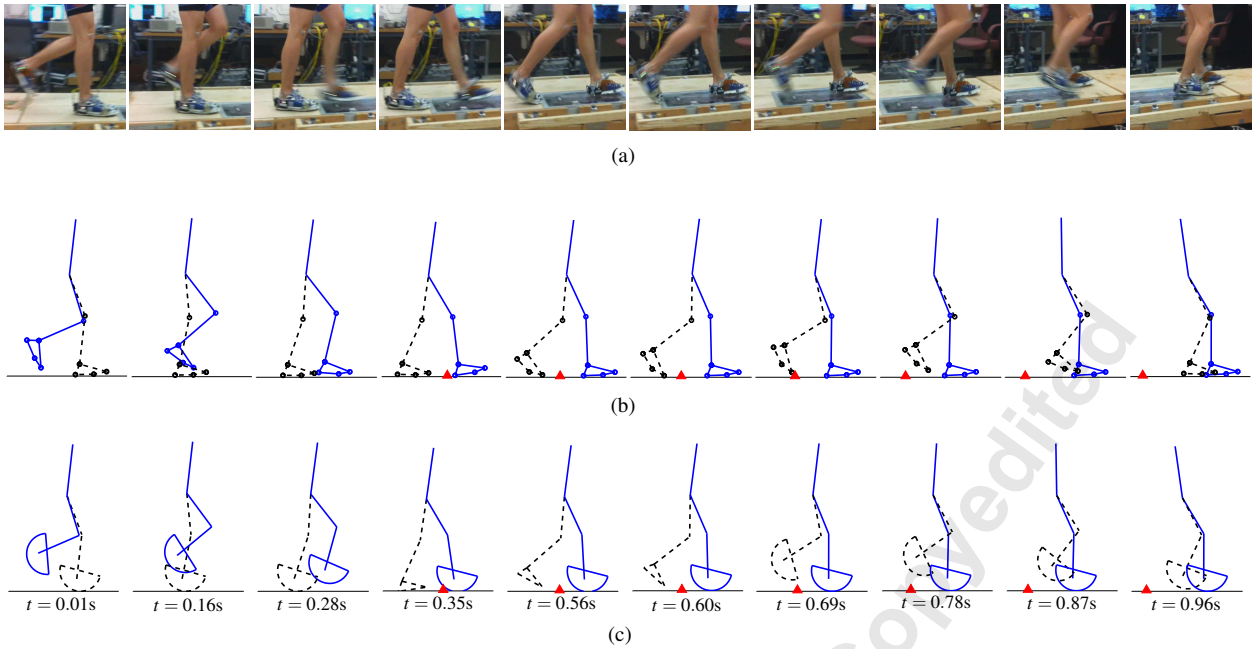


Fig. 6. A snapshot of the recovery human gait from slip. (a) Video snapshot. (b) Human 7-link skeleton from the optical motion capture system. The empty-circle dots indicate the reflective optical marker locations. (c) Skeleton prediction by the bipedal model. In (b) and (c), a red triangle is plotted to indicate the location where the left leg starts slipping. The right leg and trunk are represented by a solid blue line and the left leg by a black dash line.

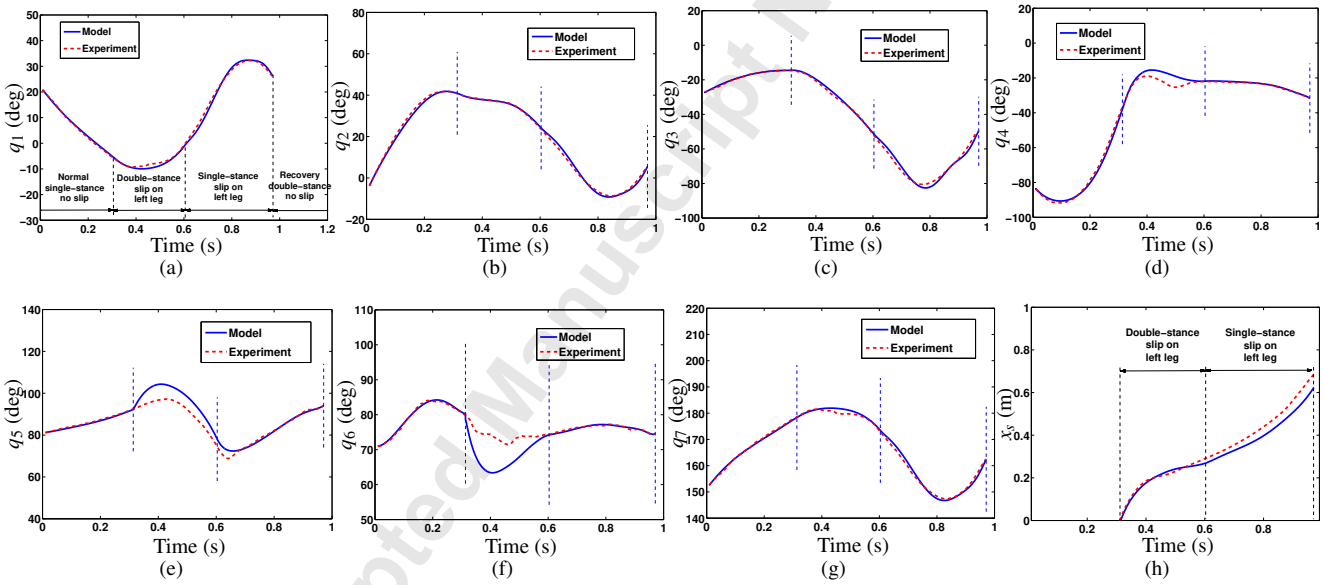


Fig. 7. (a)-(g): Joint angle ($q_1$ to $q_7$) comparisons between the model prediction and the experiments during slip recovery gait. The solid lines represent the model predictions and the dash lines show the experimental data. (h) Slipping distance $x_s$ of the (left) stance leg during the slip recovery experiment.

starts immediately when the foot touches down.

Next, we present a HZD prediction results for a multi-step slip recovery. Fig. 9 demonstrates a complete transition starting from normal walking stance (0-0.81 s), followed by a single-stance slip phase (0.81-1.28 s) and then single-stance recovery phase (1.28-2.40 s) and finally transitions back to a periodic normal walking gait. Figs. 9(a)-9(g) show the joint angle comparison results of the model prediction and experiments, while Fig. 9(h) shows the slipping distance comparison. Note that the simulation results consider only a single-stance and impact mapping neglecting double-stance. The entire recovery follows the process given in (28). The HZD model prediction results match the experiments during the slip recovery and transition to the periodic walking gait process. The slight difference in phase timings of the HZD model prediction might be due to the inaccurate parameters values used in the simulation comparing with the experiments. The simulation of the single-stance recovery phase predicts a shorter duration as compared to the experiments. We suspect that in the experiment, the subject might apply

Journal of Computational and Nonlinear Dynamics. Received August 08, 2018;
Accepted manuscript posted April 04, 2019. doi:10.1115/1.4043360


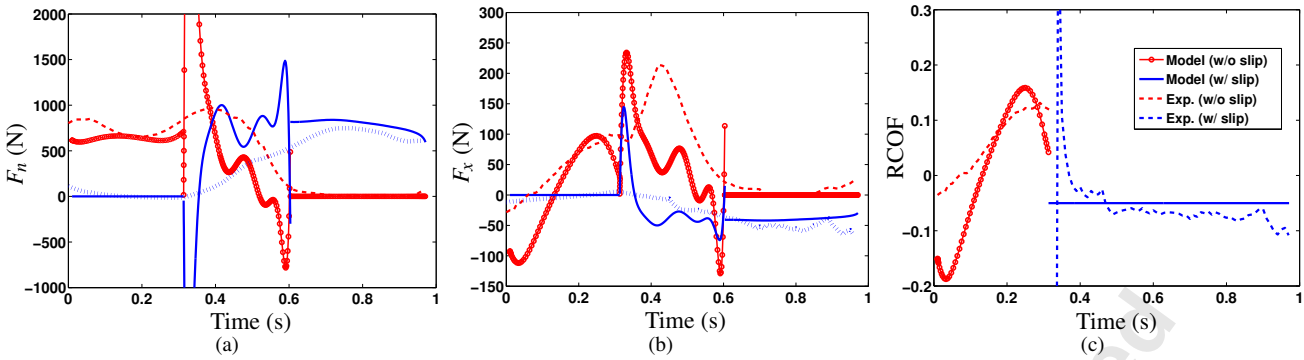


Fig. 8. Comparison results of the GRF and the required coefficient of friction (RCOF) during the slip recovery. (a) Normal GRF $F_n$. (b) Tangential GRF $F_x$. (c) RCOF of the stance leg foot. In (a) and (b), the model prediction forces for the left- and right legs are plotted as the blue solid and red circle lines, respectively, and the experiments are plotted as the blue dotted and the red dash lines. In (c), the model predicted and experimental RCOF in non-slip phase is plotted by the red empty circle and the dash lines, respectively, and these in the slip phase by the blue solid and dash lines, respectively.

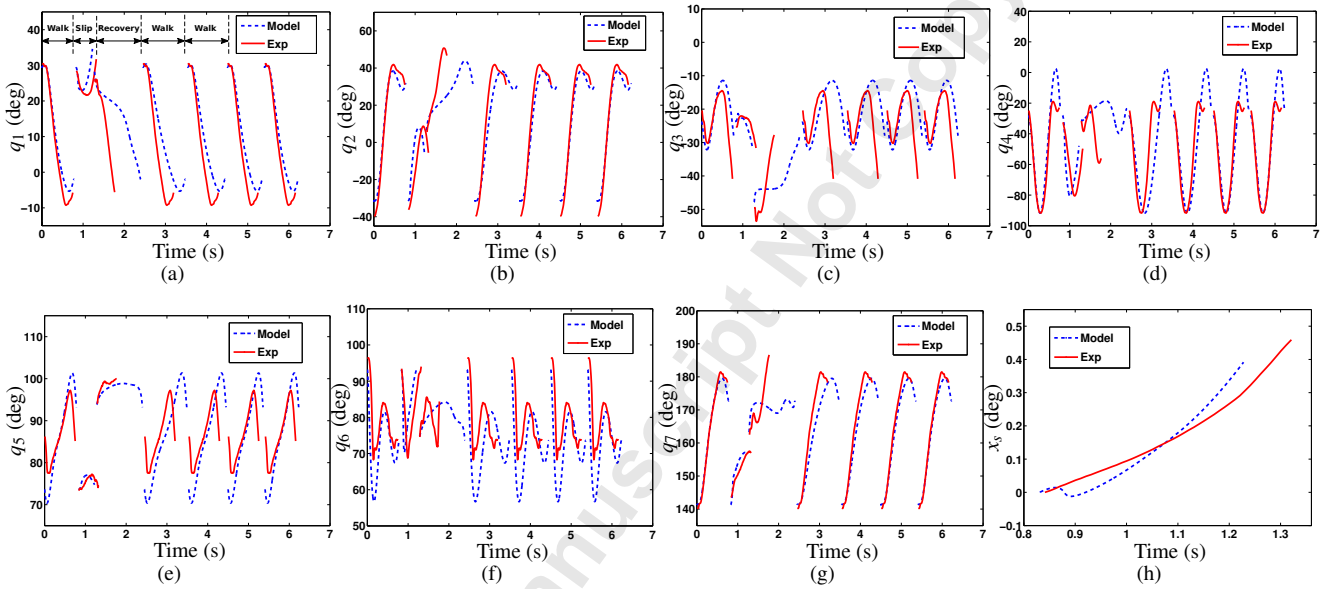


Fig. 9. (a)-(g): Joint angle ($q_1$ to $q_7$) comparisons between the HZD model prediction and the experiments during the transition from a normal walking to slip recovery and multi-step transition to a periodic walking gait. (h) Slipping distance $x_s$ of the (left) stance leg during the slip recovery experiment.

a flat foot and it can be viewed as a fully actuated inverted pendulum with ankle torque control. This ankle torque control can reshape the time constant of the used underactuated inverted pendulum model. Our simulation does not consider this effect and instead adopts circular shaped feet during the slip recovery process.

Fig. 10 shows the phase portraits of the zero dynamics for the recovery process. Fig. 10(a) illustrates the 3D phase portrait in the $\xi_1/\xi_{1s}$-$\xi_2/\xi_{2s}$-$x_s$ coordinates and Fig. 10(b) shows the phase portrait in the $\xi_1$-$\xi_2$ plane. Comparing with the normal walking gait, it is clear that the walking with foot slip generates much richer zero dynamics characteristics. The slip recovery process is on a high-dimensional manifold and consists of multiple portions of the phase portraits in 3D space as shown in Fig. 10(a). The HZD model predictions for the normal walking $\mathcal{S}_n$ (gait profile $\alpha_n$, i.e., solid blue curves) and foot-slip gait $\mathcal{S}_s$ (impact $\mathcal{H}_n^s$ and gait profile $\alpha_s$, i.e., solid red curve) match with the experiments, that is, solid blue and empty red circular markers, respectively. Moreover, as shown in Fig. 10(b), after the single-stance slip phase $\mathcal{S}_s$, the subject tried to recover from the slip by taking non-slip impact (blue dash-dot line) and then slip-to-normal recovery gait $\mathcal{S}_n(\alpha_r)$ (black dot curve for model prediction and square dots for experiments.)

In Fig. 10(b), we also mark each individual mapping $\delta_n^s$, $\Psi_s$, $\delta_s^n$, $\Phi_{\alpha_r}$, $\delta_n^n$, and $\Phi_{\alpha_n}$, which together form the composite contracting return mapping $\rho_s$ in (34) from pre-impact state $\xi_2^-$ to recovery state $\rho_s(\xi_2^-)$. These mappings clearly show the slip recovery process and also the invariant region $R$ defined by (37). We further analyze the HZD for various motions and gaits and show that the model can predict stable and unstable recovery. Fig. 11(a) shows a collection of the phase portraits of the normal walking gait, slip recovery gait and skating gaits in the $\xi_{1s}$-$\xi_{2s}$-$x_s$ space. The steady skating

Journal of Computational and Nonlinear Dynamics. Received August 08, 2018;
Accepted manuscript posted April 04, 2019. doi:10.1115/1.4043360


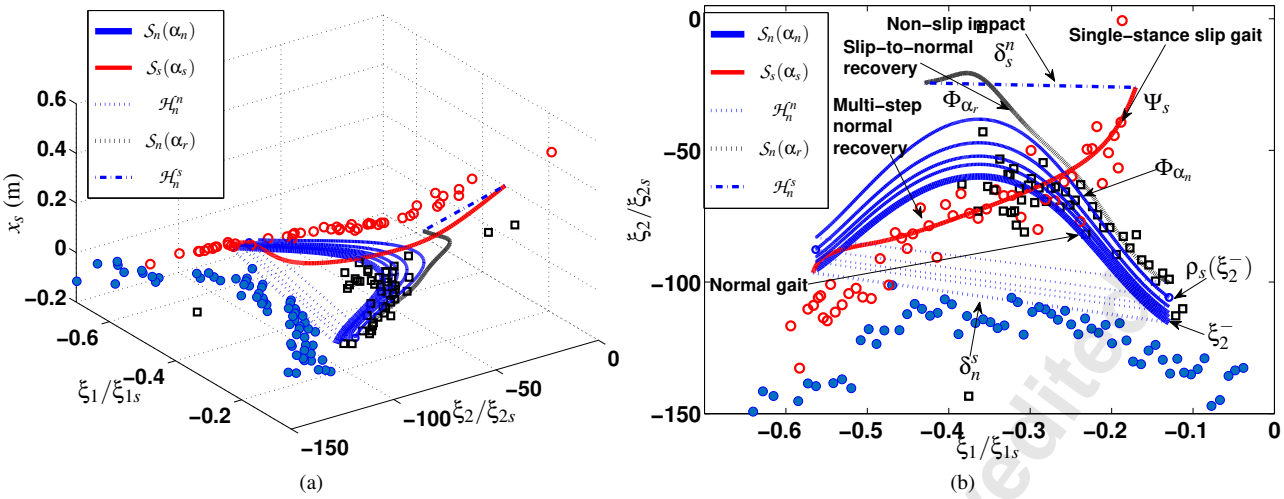


Fig. 10. (a) 3D phase portrait ($\xi_1/\xi_{1s}$-$\xi_2/\xi_{2s}$-$x_s$) during the slip recovery process. (b) 2D phase portrait in $\xi_1/\xi_{1s}$-$\xi_2/\xi_{2s}$ plane. In both plots, the empty circles and the empty squares are the experimental data during the phases $\mathcal{H}_n^s$ and $\mathcal{H}_s^r$, respectively. The solid circles are experimental data during normal walking phase $\mathcal{S}_n$ with gait profile $\alpha_n$.

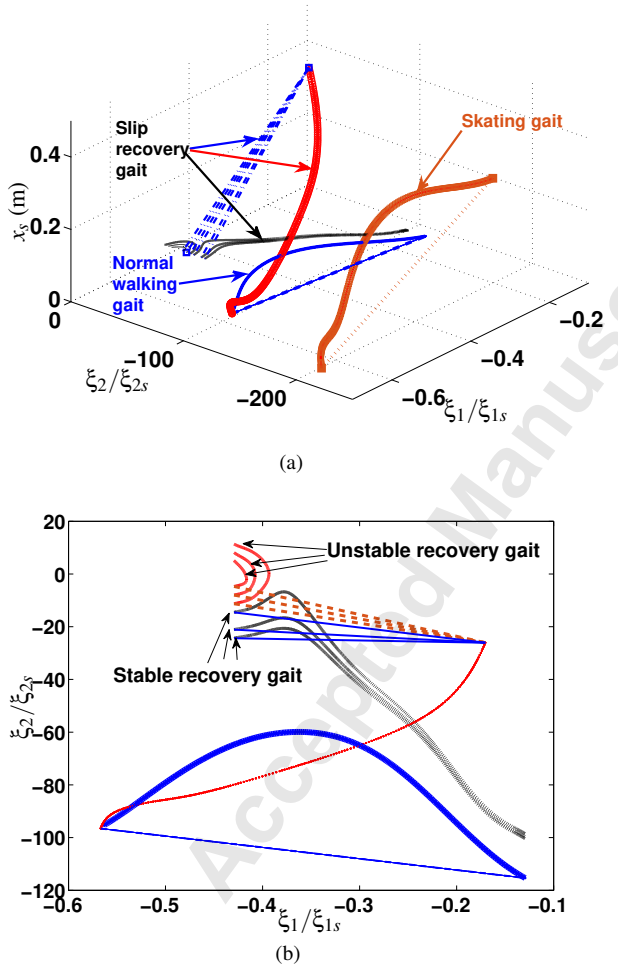


Fig. 11. (a) Phase portraits of the normal walking gait, slip recovery gait, and skating gaits in 3D space. (b) Phase portrait of the successful and unsuccessful slip recovery gaits in the $\xi_1/\xi_{1s}$-$\xi_2/\xi_{2s}$ plane.

gait is generated by considering both slipping and walking gaits as the skilled human motor locomotion. It is clear that the zero dynamics of the normal walking gait are located in the $\xi_1$-$\xi_2$ plane, while the skating gait is in the 3D space with motion in the $x_s$ direction. The slip recovery gait consists of a series of transient motion that deviates from and then returns to the normal walking gaits. Fig. 11(b) further illustrates the slip recovery gaits in which both successful, stable recovery (blue and black curves) and unsuccessful, unstable recovery (dash and solid red curves) gaits are plotted. Both sets of recovery gaits are obtained by enforcing the same virtual constraints. The only difference between these two trajectories is the value of $b_n$ in (7) of the impact from slip gait to recover gait. The difference of $b_n$ in (7) gives different initial $\xi_2$ values for the recovery gait, which indicates the falling angular moments. Once the value of $\xi_2$ passes through zero and becomes positive, the progression variable $\xi_1 = \theta$ is in a decreasing trend and this implies that the gait cannot be completely recovered. Fig. 6(c) demonstrates the gait profiles for a successful slip recovery.

## 6 Discussion

One of the main goals of this study was the development of a bipedal model for analytical analysis of slip balance recovery. We recruited a single subject in our experiments and that is sufficient to serve the validation of the model development. The bipedal model and analysis can be applied to study walking and slip gait of any subject for whom the kinematic data is known. The model parameters (i.e., link lengths and masses) and joint angle trajectories are subject specific and need to be tuned for each individual. This paper does not provide generalization of slip balance recovery strategies across a wide population, since this would require analysis of multi-subject slip balance recoveries and is out of the scope of this paper.

During normal walking, the deviation between model

and experimental results of the ankle angle ($q_6$) trajectory (see Fig. 4(g)) is primarily due to the approximation of using curved feet compared to the realistic human feet that have multi-DOFs. The circular feet can only roll on the ground and have a single point contact that coincides with the COP location. This is different compared to the human foot, which during single stance phase lays flat while COP progresses forward. These differences reflect also in the GRF profiles as shown in Fig. 5, where discrepancies between the model and experimental results exist primarily during double stance phase. At that instant, the toes of the swing (trailing) foot push-off the ground and generate additional forces, while the circular foot only rolls forwards and does not have these capabilities. These differences originate from the discrepancies between the actual foot-floor rollover shape and circular foot approximation during the end of the stance as shown in Fig. 4(a). The differences between the model's rigid circular foot and the human's flexible foot complicate exact matching of the ankle angles during double stance slip phase. Slip occurrence during that phase further complicates exact matching. Use of circular foot was validated to be a reasonable approximation but however, it is impossible to guarantee exact matching of all the joint angles throughout the whole stance, due to the reduced number of degrees of freedom compared to the human anatomical foot. The differences between foot orientation in the experiments and the model's circular foot in Fig. 6 are due to the reason that the model's circular foot is rolling on the ground and has a point contact, compared to the human foot that can lay flat on the ground while changing location of a COP within the foot support.

The limitation of this work is that the model considers only sagittal plane motion. While this captures the most important walking and slip characteristic, inclusion of motion and foot placement in a lateral plane can further explain overall slip balance recovery and provides a complete analysis of the human response during slip perturbations.

## 7 Conclusions and Future Work

This paper presented a robotic bipedal dynamic model and the extended hybrid zero dynamics (HZD) for human walking gait with foot slip. We relaxed the non-slip assumption used in the existing bipedal robotic models and explicitly modeled the foot slipping on the ground. A general hybrid bipedal model and the gait controllers were developed for human walking with foot slip. The presented HZD was an extension of the existing dynamics for normal walking locomotion. We explicitly derived and presented the HZD for human walking with foot slip that contains two additional zero dynamics states. It is interesting to show that the HZD under foot slip presented rich human motor skills, including the normal walking, slip recovery gaits and highly skilled skating motion. Stability condition for slip recovery gait was discussed and the HZD-based recovery simulation and experiments were also successfully demonstrated.

We plan to extend the HZD model to further analyze the motion stability and dependency on the model parameters and motion variables. We are also working on how to design virtual gait constraints and slip recovery strategies that can lead to stable HZD under foot slip. Integration of the modeling and analysis of the stable HZD and the gait control under foot slip with robotic assistive devices is another future research direction.

## Acknowledgements

The work was partially supported by NSF under awards CMMI-1334389 and CMMI-1762556. The authors thank the members of the Robotics, Automation and Mechatronics (RAM) Lab at Rutgers for their help.



## References

[1] Stevens, J. A., Corso, P. S., Finkelstein, E. A., and Miller, T. R., 2006. "The costs of fatal and non-fatal falls among older adults". *Inj. Prev.,* **12**, pp. 290–295.

[2] Burns, E. R., Stevens, J. A., and Lee, R., 2016. "The direct costs of fatal and non-fatal falls among older adults–United States". *J. Safety Res.,* **58**, pp. 99–103.

[3] Bureau of Labor Statistics, Nov. 2016. US Department of Labor.

[4] Redfern, M. S., Cham, R., Gielo-Perczak, K., Grönqvist, R., Hirvonen, M., Lanshammar, H., Pai, C. Y.-C., and Power, C., 2001. "Biomechanics of slips". *Ergonomics,* **44**(13), pp. 1138–1166.

[5] Yang, F., and Pai, Y.-C., 2010. "Reactive control and its operation limits in responding to a novel slip in gait". *Ann. Biomed. Eng.,* **38**(10), pp. 3246–3256.

[6] Patton, J., Pai, Y.-C., and Lee, W. A., 1999. "Evaluation of a model that determines the stability limits of dynamic balance". *Gait & Posture,* **9**, pp. 38–49.

[7] Mahboobin, A., Cham, R., and Piazza, S. J., 2010. "The impact of a systematic reduction in shoe-floor friction on heel contact walking kinematics - A gait simulation approach". *J. Biomech.,* **43**, pp. 1532–1539.

[8] Dingwell, J. B., and Kang, H. G., 2007. "Differences between local and orbital dynamic stability during human walking". *ASME J. Biomech. Eng.,* **129**, pp. 586–593.

[9] Westervelt, E. R., Grizzle, J. W., Chevallereau, C., Choi, J. H., and Morris, B., 2007. *Feedback control of dynamic bipedal robot locomotion*. CRC Press, Boca Raton, FL.

[10] Grizzle, J. W., Chevallereau, C., Sinnet, R. W., and Ames, A. D., 2014. "Models, feedback control, and open problems of 3D bipedal robotic walking". *Automatica,* **50**(8), pp. 1955–1988.

[11] Srinivasan, S., Raptis, I. A., and Westervelt, E. R., 2008. "Low-dimensional sagittal plane model of normal human walking". *ASME J. Biomech. Eng.,* **130**, pp. 051017–1–051017–11.

[12] Martin, A. E., and Schmiedeler, J. P., 2014. "Predicting human walking gaits with a simple planar model". *J. Biomech.,* **47**, pp. 1416–1421.

[13] Srinivasan, S., 2007. "Low-dimensional modeling and analysis of human gait with application to the gait of

transtibial prosthesis users". PhD thesis, Dept. Mech. Eng., Ohio State Univ., Columbus, OH.

[14] Hansen, A. H., Childress, D. S., and Knox, E. H., 2004. "Roll-over shapes of human locomotor systems: Effects of walking speed". *Clin. Biomech.,* **19**(4), pp. 407–414.

[15] Westervelt, E. R., Grizzle, J. W., and Koditschek, D. E., 2003. "Hybrid zero dynamics of planar biped walkers". *IEEE Trans. Automat. Contr.,* **48**(1), pp. 42–56.

[16] Chen, K., Trkov, M., Yi, J., Zhang, Y., Liu, T., and Song, D., 2015. "A robotic bipedal model for human walking with slips". In Proc. IEEE Int. Conf. Robot. Autom., pp. 6301–6306.

[17] Chen, K., Trkov, M., and Yi, J., 2017. "Hybrid zero dynamics of human biped walking with foot slip". In Proc. Amer. Control Conf., pp. 2124–2129.

[18] Grönqvist, R., Chang, W.-R., , Courtney, T. K., Leamon, T. B., Redfern, M. S., and Strandberg, L., 2001. "Measurement of slipperiness: Fundamental concept and definitions". *Ergonomics,* **44**(13), pp. 1102–1117.

[19] Kong, K., and Tomizuka, M., 2009. "A gait monitoring system based on air pressure sensors embedded in a shoe". *IEEE/ASME Trans. Mechatronics,* **14**(3), pp. 358 –370.

[20] Liu, T., Inoue, Y., Shibata, K., and Shiojima, K., 2012. "A mobile force plate and three-dimensional motion analysis system for three-dimensional gait assessment". *IEEE Sensors J.,* **12**(5), pp. 1461–1467.

[21] Trkov, M., Yi, J., Liu, T., and Li, K., 2018. "Shoe–floor interactions in human walking with slips: Modeling and experiments". *ASME J. Biomech. Eng.,* **140**(3), pp. 031005–1–031005–11.

[22] Zhang, Y., Chen, K., Yi, J., and Liu, L., 2014. "Pose estimation in physical human-machine interactions with application to bicycle riding". In Proc. IEEE/RSJ Int. Conf. Intell. Robot. Syst., pp. 3333–3338.

[23] Chevallereau, C., Djoudi, D., and Grizzle, J. W., 2008. "Stable bipedal walking with foot rotation through direct regulation of the zero moment point". *IEEE Trans. Robotics,* **24**(2), pp. 390–401.

[24] Braun, D. J., and Goldfarb, M., 2009. "A control approach for actuated dynamic walking in biped robots". *IEEE Trans. Robotics,* **25**(6), pp. 1292–1303.

[25] Zhao, H.-H., Ma, W.-L., Zeagler, M. B., and Ames, A. D., 2014. "Human-inspired multi-contact locomotion with AMBER2". In Proc. ACM/IEEE Int. Conf. Cyber-Phys. Syst.

[26] Spong, M. W., Hutchinson, S., Vidyasagar, M., et al., 2006. *Robot modeling and control*, Vol. 3. John Wiley & Sons, Inc., New York, NY.